International Journal of Nanomedicine

Dovepress
Taylor & Francis Group

Open Access Full Text Article

ORIGINAL RESEARCH

Biomimetic Aggregation-Induced Emission Luminogens Mediated Effective Phototherapy and Immune Checkpoint Blockade for the Synergistic Treatment of Lung Cancer

Langyu Yang[1,2,*], Minyan Wei[1,2,*], Xiaohua Deng[1,2,*], Linlong He[1,2], Yinshan Lin[1,2], Xufeng Lin[1,2], Dazhi Zhou[1,2], Ming Li[3], Aiping Qin[1,2], Lingmin Zhang[1,2], Zizhang Ouyang[1]

[1]The Affiliated Qingyuan Hospital (Qingyuan People's Hospital), Guangzhou Medical University, Qingyuan, Guangdong, 511518, People's Republic of China; [2]The Affiliated Panyu Central Hospital, The Fifth Affiliated Hospital, Guangzhou Municipal and Guangdong Provincial Key Laboratory of Molecular Target & Clinical Pharmacology, the NMPA and State Key Laboratory of Respiratory Disease, AIE Pharmaceutical Biology Innovation Research Center, School of Pharmaceutical Sciences, Guangzhou Medical University, Guangzhou, 511436, People's Republic of China; [3]Medical Research Center, The Affiliated Guangdong Second Provincial General Hospital of Jinan University, Jinan University, Guangzhou, Guangdong, 510317, People's Republic of China

*These authors contributed equally to this work

Correspondence: Lingmin Zhang; Zizhang Ouyang, Email zhanglm@gzhmu.edu.cn; 2019695272@gzhmu.edu.cn

Background: Lung cancer has become one of the most fatal cancers at present. Traditional treatments showed limited therapeutic effects on lung cancer. The phototherapy has emerged as a powerful approach for lung cancer treatment. Aggregation-induced emission luminogens (AIEgens) exhibit excellent optical performance such as strong fluorescence, enhanced reactive oxygen species (ROS) generation, and effective thermal effect after aggregation, which show great potential in phototherapy. However, the disadvantages including hydrophobicity, low specificity, and short circulation lifetime limited their efficacy on cancer therapy.

Methods: We developed a biomimetic AIEgens constructed using $CD8^+$ T cells membrane to camouflage the AIEgen $C_{41}H_{37}N_2O_3S_2$ (named BITT) nanoparticles (termed TB). The prepared TB improved the tumor accumulation of AIEgen by PD-1/PD-L1 recognition on the $CD8^+$ T and LLC cell membranes, respectively.

Results: The prepared TB showed improved binding efficiency, photothermal effects, and ROS generation ability to kill the lung cancer cells. TB also showed improved circulation lifetime and excellent tumor targeting ability, leading to effective phototherapy and immunotherapy in vivo based on BITT and the $CD8^+$ T cell-derived membranes. Based on the AIE and immune checkpoint blockade (ICB) strategies, TB enhanced the antitumor activities of lung cancer by phototherapy and immunotherapy.

Conclusion: The present work developed a type of biomimetic AIEgens, which overcame the inherent limitations of conventional AIEgens and leveraged immune recognition for targeted tumor accumulation. Furthermore, the integration of AIE-driven phototherapy with immune checkpoint blockade demonstrated potent synergistic antitumor efficacy, establishing a promising combinatorial strategy against aggressive lung malignancies.

Keywords: aggregation-induced emission luminogens, T cells, phototherapy, immune checkpoint blockade, lung cancer

Introduction

Lung cancer has become one of the most fatal cancers at present,[1,2] which leads to a 5-year survival rate of less than 15%.[3] Traditional treatments such as surgery, chemotherapy, and radiation therapy showed limited therapeutic effects on lung cancer.[4] It is in great demand to develop novel strategies to improve the therapeutic effects. Phototherapy, including photothermal therapy (PTT) and photodynamic therapy (PDT), has shown powerful effects on cancer therapy, which is highlighted by the advantages such as high specificity, non-invasiveness, and negligible drug resistance compared to

Received: 5 June 2025
Accepted: 14 August 2025
Published: 24 August 2025

conventional cancer treatments.[5] The Jablonski diagram indicates that when a photosensitizer molecule is excited by absorbing a photon, the excited electrons in the photosensitizer are unstable and dissipate energy through fluorescence, thermal, and intersystem crossing transition with energy releasing, which generates phosphorescence or interacts with surrounding substances like oxygen and H_2O to generate ROS including various cytotoxic oxygen radicals (such as superoxide anion radicals (•O- 2), hydroxyl radicals (•OH), and hydrogen peroxide (H_2O_2)) and the singlet oxygen ($^1O_2$).[6,7] The effects can be used for fluorescence imaging, PTT, or PDT, respectively.[8] The effective phototherapy is largely dependent on the photosensitizers.[9] However, conventional photosensitizers are limited to their aggregation-caused quenching behavior, resulting in weakened fluorescence emission and reduced ROS generation in the aggregated form.[10] The disadvantages have seriously restricted the application of PTT in cancer diagnosis and treatment.

The aggregation-induced emission luminogens (AIEgens) were considered favorable photosensitizers for diagnosis and treatment, which have recently become popular in biomedical applications.[11–13] Different from the conventional photosensitizers, AIEgens exhibit intense emission and enhanced ROS generation when aggregated.[14,15] Beneficial from this unique photophysical phenomenon, AIEgens show better imaging or phototherapy performances than conventional photosensitizers under light irradiation, which is useful in the theranostics of cancer.[16] Recently, a novel AIE active zwitterionic compound $C_{41}H_{37}N_2O_3S_2$ (named BITT) was successfully synthesized.[17] BITT nanoparticles exhibited excellent aggregation-induced emission (AIE) characteristics, good photothermal stability, and effective reactive oxygen species generation capacity, which could provide superior fluorescence imaging and photothermal/photodynamic performance on cancer diagnosis and treatment.[18] Nevertheless, several problems might still need to be solved for further application. BITT nanoparticles for phototherapy might be limited by their hydrophobic nanostructure and poor tumor accumulation.[19] The limited tissue permeability might also decrease the fluorescence imaging ability and photothermal/photodynamic effect. Thus, the improvement of the surface properties may endow the AIEgen with enhanced tumor-targeting ability and high tissue permeability, which is beneficial for the treatment of lung cancer.

Cell membrane coating technology has been a useful strategy to improve the surface function of nanoparticles for precise cancer therapy.[20–22] These nanoparticles functionalized with cell membranes leveraged the intrinsic characteristics of nanoparticles and unique functionalities of natural cells, facilitating their stability, long circulation, and improved accumulation in the tumors.[23–25] $CD8^+$ T cells are considered as one of the T lymphocytes for mediating adaptive immune responses, which play important roles in immunotherapy.[26–28] However, the programmed cell death protein 1 (PD-1), which is highly expressed on the activated $CD8^+$ T cells, can specifically target programmed cell death ligand 1 (PD-L1) expressed on tumor cells and help tumor cells evade immune surveillance.[29–31] As a result, the T cell-mediated cancer-killing effect might be suppressed by the interaction between PD-1 and PD-L1.[32] Furthermore, $CD8^+$ T cell membrane's phospholipid bilayer inherently improves nanoparticle hydrophobicity by providing an amphiphilic interface: its outer leaflet, enriched with hydrophilic phosphorylcholine headgroups and glycolipids, masks the nanoparticle's core hydrophobicity through biomimetic surface hydration, while the inner hydrophobic fatty acid tail region interfaces directly with hydrophobic nanoparticle surfaces via lipophilic interactions. This structural duality simultaneously enhances water compatibility through the membrane's hydrophilic exterior and stabilizes hydrophobic nanoparticle cores via the lipid tails' affinity, effectively shielding hydrophobic domains and improving colloidal stability without compromising membrane protein functionality like PD-1/PD-L1 targeting.[33,34] Inspired by the facts mentioned above, the biomimetic nanoparticles coating with PD-1 overexpressed $CD8^+$ T cell membrane could specifically target the tumor cells by blocking the immune checkpoint ligand PD-L1. Biomimetic nanoparticles decorated with $CD8^+$ T cell membrane might accumulate on tumor cells with the PD-1 and PD-L1 interaction and reactivate the endogenous T cell-mediated immune response by immune checkpoint blockade. Hence, the $CD8^+$ T cell membrane decoration on BITT might endow good tumor-targeting ability and high tissue permeability for BITT, and enhance superior photothermal efficiency and antitumor immunity in lung cancer therapy.

In the present work, a type of biomimetic AIEgen (termed TB) was developed for efficient phototherapy and immunotherapy on lung cancer based on the AIE and ICB strategies. In this biomimetic platform, the AIEgen BITT nanoparticles were used as the core and severed as an excellent photosensitizer for photothermal and photodynamic efficacy. To amplify the photothermal/photodynamic efficacy and activate the antitumor immunity, BITT nanoparticles were camouflaged with $CD8^+$ T cells membrane (Scheme 1). TB was expected to accumulate in the lung cancer cells with the PD-1 and PD-L1 interaction, then would enhance the photothermal effects and ROS efficacies with the AIE characteristic, and synergistically

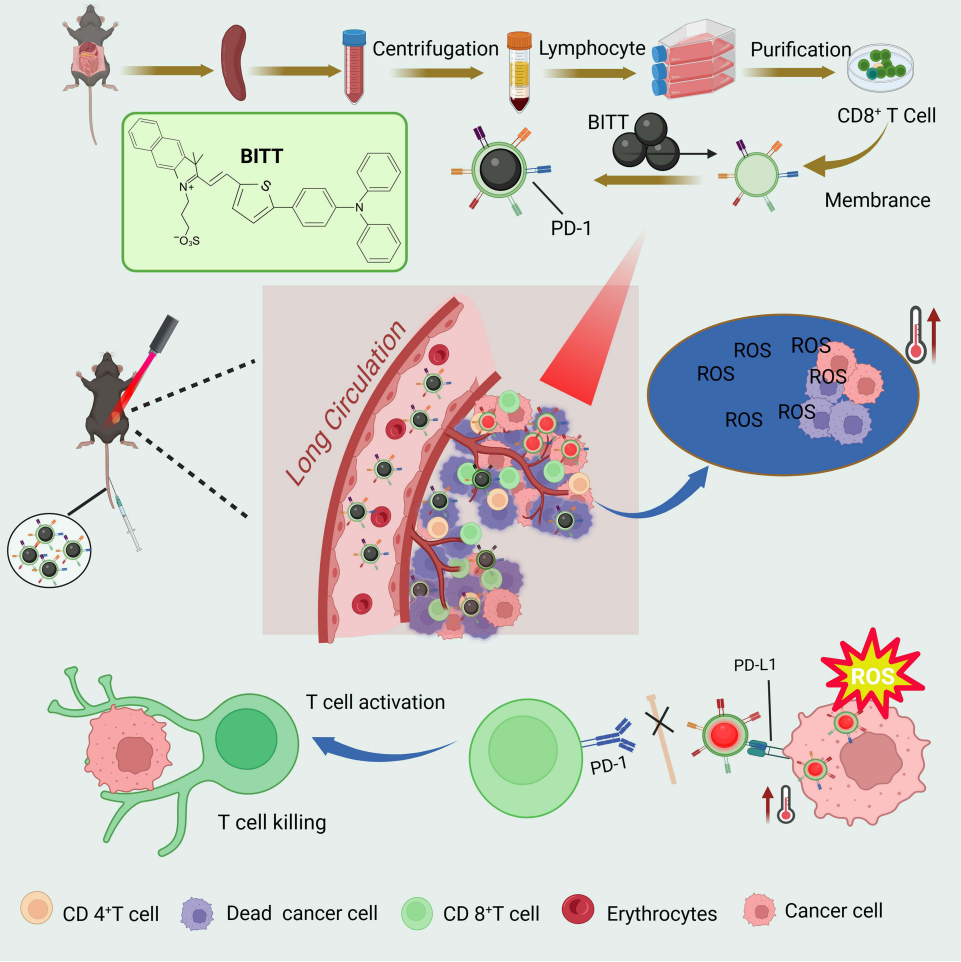

Scheme 1 The preparation of TB and the cancer therapy induced by TB. TB, $CD8^+$ T cells membsranes/BITT.
Abbreviations: PDT, photodynamic therapy; PTT, photothermal therapy; ICB, immune checkpoint blockade.

exert intrinsic immune activation by immune checkpoint blockade (Scheme 1). Furthermore, the AIEgen BITT developed in this study exhibited both photodynamic and photothermal properties, allowing synergistic phototherapy without the need for multiple agents or complex formulations. This research not only eliminated the primary tumor but also activates the immune response in the tumor microenvironment, thereby further expanding its therapeutic potential.

Materials and Methods

Materials

2′,7′-dichlorodihydrofluorescein diacetate (DCFH-DA) was purchased from Sigma-Aldrich (St. Louis, USA). Fetal bovine serum (FBS), Roswell Park Memorial Institute (RPMI-1640) medium, Dulbecco's modified Eagle medium (DMEM) medium, and trypsin were purchased from Gibco. The antibiotics (penicillin and streptomycin), phosphate-buffered saline (PBS), CCK-8, Calcein-AM/PI double stain kit, Actin-488, and Hoechst 33342 were purchased from Beyotime Biotechnology. BITT was obtained from Xi'anruixi Biological Technology Co., Ltd. All other reagents were purchased from commercial suppliers without further purification.

Extraction and Identification of $CD8^+$ T Cells

Male C57BL/6 mice were anesthetized with 5% isoflurane and sacrificed. The spleens were collected from mice and washed with HBSS (Hank′s balanced salt solution). Then the spleen was chopped and digested with the digestive enzymes, shaken at 37°C for 60 min, and filtered through a 300-mesh filter. Finally, the filtered mixture was collected and

https://doi.org/10.2147/IJN.S536484

resuspended in a complete RPMI 1640 medium. The mouse T lymphocyte cells were isolated from the spleens of normal C57BL/6 mice with Lymphoprep (STEMCELL Technologies Inc., Vancouver, BC, Canada), following the manufacturer′s instructions. Mouse T lymphocyte cells were maintained in RPMI 1640 medium supplemented with 10% FBS and 1% antibiotics (penicillin/streptomycin). $CD8^+$ T cells were purified by EasySep™ Mouse CD8+ T Cell Isolation Kit (STEMCELL Technologies Inc., Vancouver, BC, Canada). The harvested T cells were stained with fluorochrome-conjugated antibodies against CD3, CD8, PD-1, and CD45, and analyzed on a flow cytometry analyzer (BD LSR Fortessa, BD, CA). Furthermore, $CD8^+$ T cells were incubated with Phorbol-12-myristate-13-acetate (50 ng/mL) and Ionomycin (1 μg/mL) at 37°C for 4 h. The cells were collected and stained with flow cytometry antibodies including CD8 and CD69. To detect the PD-L1 on the LLC cells, the flow cytometry antibodies PD-L1 and TTF1 were used to stain the LLC cells.

Preparation of BITT Nanoparticles

BITT nanoparticles were prepared according to the previous study with minor modifications.[17] In brief, the BITT solution (1.0 mg/mL in DMSO, 2 mL) was added dropwise into 18 mL of deionized water under sonication (Scientz-IID sonicator, Scientz Biotechnology Co., Ltd., Ningbo, China) for 5 min. Then, free BITT was removed by dialysis (MWCO:14000 Da) in deionized water for 24 h. Finally, BITT nanoparticles were concentrated by ultrafiltration and stored at 4°C before use.

Preparation of TB

T cell membrane-coated BITT (TB) was prepared according to the previous study.[19] Firstly, the T cell membrane (CM) was extracted from T cells by a membrane protein extraction kit, following the instructions from the manufacturer (Biyotime, China). The obtained T cell membrane was suspended in PBS and sonicated by a Scientz-IID ultrasonicater (Scientz Biotechnology, China). The bicinchoninic acid (BCA) method was applied to determine the concentration. The cell membranes were stored at −80°C until use.

To coat the BITT nanoparticles with $CD8^+$ T cell membranes, BITT nanoparticles were mixed with cell membranes at different weight ratios, and sonicated for 1 h by a Scientz IID ultrasonicater (Scientz Biotechnology, China). Finally, the mixture was extruded through the 200 and 100 nm polycarbonate membrane using a mini extruder (Avanti, Canada) 20 times.

Characterization of TB

The particle size and morphology of TB were observed on a JEM-100XII transmission electron microscope (TEM, JEOL, Japan). Particle sizes, size distribution, and zeta potential of TB were analyzed on a Malvern Zeta sizer Nano ZS90 measurement (Malvern, UK) at room temperature via the dynamic light scattering method (DLS). UV absorption spectra of BITT and TB (20 μg/mL BITT in water) were measured on a UV-2600 UV-Vis spectrophotometer (SHIMADZU, Japan). Fluorescence spectra of BITT and TB (BITT at a dosage of 20 μg/mL) were measured with an emission wavelength of 534 nm on a fluorescence spectrophotometer (Hitachi, Japan). Fluorescence spectra of BITT and TB (20 μg/mL BITT in water) were also measured with an excitation wavelength of 730 nm on a fluorescence spectrophotometer (Hitachi, Japan). SDS-PAGE gel electrophoresis assay was displayed for the protein characterization.

Detection of TB Nanoparticles by Singlet Oxygen Sensor Green (SOSG) Probe

Different formulations (BITT equivalent to 20 μg/mL) were incubated with singlet oxygen sensor green (SOSG) probe (5 μM) and exposed to 658 nm laser for 5 min with the power of 2 $W{\cdot}cm^{-2}$. PBS was used as control. The emission spectrums range were scanning at Ex = 504 nm with fluorescence spectrophotometer (Hitachi, Japan).

Photothermal Performance and Photothermal Stability of TB

To evaluate the photothermal conversion behavior, the water solutions of BITT and TB (BITT at a dosage of 20 μg/mL) were continuously exposed to a 658 nm laser irradiation with a power density of 1 or 2 $W{\cdot}cm^{-2}$ for 6 min, respectively. The temperature was measured every 10s and stopped until the temperature nearly arrived at a plateau. For the photothermal stability studies, the water solutions of BITT and TB (BITT at a dosage of 20 μg/mL) were irradiated

under a 658 nm laser irradiation at 2 $W \cdot cm^{-2}$, respectively. The temperatures of the samples were measured in six circles of heating and cooling process. During one heating and cooling cycle, the samples were irradiated with a 658 nm laser for the first 5 min to reach a steady state. Following the removal of the laser irradiation, the samples were allowed to cool down naturally to the ambient temperature for 5 min.

Thermal Imager Observed the Temperature of BITT in the Solution

Different formulations (BITT equivalent to 20 μg/mL) were exposed to 658 nm laser for 5 min with the power of 2 $W \cdot cm^{-2}$. The temperatures were monitor by FLUKE Ti480u thermal infrared imager.

Cell Culture

Mouse Lewis lung carcinoma (LLC) cells were purchased from the Shanghai Institute of Cell Biology, Chinese Academy of Sciences (Shanghai, China). LLC cells were cultivated in RPMI1640 supplement with 10% fetal bovine serum and 1% antibiotics (penicillin/streptomycin) and maintained at 37°C in a humidified atmosphere with 5% CO_2.

Binding Efficiency

LLC cells with a density of 1×10^5 cells/well were seeded in confocal imaging dishes and cultured for 24 h. Then, LLC cells were incubated for 6 h with TB at various BITT concentrations (5, 10, 15, and 20 $\mu g \cdot mL^{-1}$), respectively. LLC cells treated with TB (20 $\mu g \cdot mL^{-1}$) were also incubated for different hours (1, 3, 6, and 9 h). After that, the treated LLC cells were washed with PBS three times. For confocal imaging, the treated cells were stained with Hoechst 33342 for 30 min. The cellular images were observed by a Zeiss LSM 880 confocal microscope (Zeiss, USA). For FACS analysis, the treated cells were trypsinized, collected, and analyzed with a flow cytometer (Becton Dickinson, USA). LLC cells without treatment were chosen as the negative control.

PD-L1 Inhibitor BMS-1 Verify the Binding of PD-1/PD-L1

LLC cells with a density of 5×10^4 cells per well were seeded into confocal imaging dishes and cultured for 24 h. And then added the 5 μM BMS-1 to LLC cells and co-culture at 37°C for 2 h. Subsequently, the nanoparticles containing BITT from different groups were co-cultured for 9 h. After washing with PBS, the fluorescence of BITT was observed using confocal microscopy.

Cytotoxicity Study

The cytotoxicity of TB was performed on LLC cells by the CCK-8 method. In brief, LLC cells with a density of 5×10^3 cells per well were seeded into 96-well plates and cultured for 24 h. Then, the LLC cells were incubated with different concentrations of BITT in fresh media for 9 h. Afterward, the BITT-treated cells were exposed to laser irradiation (2 $W \cdot cm^{-2}$) for 5 min. Meanwhile, the BITT-treated cells without light irradiation were also conducted for the dark cytotoxicity study. After further incubation for 2 h, the treated cells were washed with PBS and then incubated with fresh medium containing 10% CCK-8 at 37°C for another 4 h. Finally, the absorbance was measured at a wavelength of 450 by a microplate reader (Thermo, USA). The relative cell viability was calculated after different treatments. The cells without any treatment were chosen as the control.

Live/Dead Staining

LLC cells with at a density of 1×10^5 cells per well were seeded into 24-well plates and cultured for 24 h. Then, LLC cells were incubated with PBS, BITT, and TB (BITT, 20 $\mu g \cdot mL^{-1}$) for 9 h, respectively. After that, the treated cells were exposed to the laser irradiation (2 $W \cdot cm^{-2}$) for 5 min. Meanwhile, the treated cells without light irradiation were also conducted as the negative controls. After 2 h incubation, the cells were stained with a Calcein-AM/PI Double Stained Kit (Biyuntian, China) for 10 min. Finally, the treated cells were washed with PBS and imaged by an inverted fluorescent microscope (Leica, Japan).

Intracellular ROS Generation

LLC cells with at a density of 1×10^5 cells per well were seeded into confocal imaging dishes and cultured for 24 h. Then, the cells were incubated with PBS, BITT, and TB (20 μg·mL^{-1} BITT) in the dark for 6 h, respectively. DCFH-DA was added, and the cells were incubated at 37°C for 20 min. After washing with PBS, the treated cells were exposed to laser irradiation (2 W·cm^{-2}) for 5 min, followed by CLSM imaging. The treated cells without laser irradiation were chosen as the negative controls.

Penetration of TB Into Lung 3D in vitro Tumor Spheroid Model

The in vitro lung 3D tumor spheroid model was established according to the previous method.[19] When the lung 3D tumor spheroid reached a size of 100 μm, PBS, BITT, and TB (20 μg·mL^{-1} BITT) were added and penetrated the tumor spheroids in the dark at 37°C for 6 h, respectively. After that, the treated tumor spheroids were exposed to laser irradiation (2 W·cm^{-2}) for 5 min. After 2 h incubation, the tumor spheroids were stained with a Calcein-AM/PI Double-Stained Kit (Beyotime Biotechnology, China) for 10 min. Finally, the tumor spheroids were washed with PBS and imaged by CLSM. The treated tumor spheroids without laser irradiation were chosen as the negative controls.

Animals and Tumor-Bearing Mouse Model

The male C57BL/6 mice at 6–8 weeks old (20 g weight per mouse) were obtained from Shanghai Slac Laboratory Animal Co. Ltd (Shanghai, China). We performed the animal studies according to the Guide for the Care and Use of Laboratory Animals published by US National Institutes of Health (No. 85–23, 1996). All the animal experiments were performed by the protocols approved by the Institutional Animal Care and Use Committee of Guangzhou Medical University (GY2022-024). To establish the LLC tumor-bearing mice model, LLC cells (2×10^6 cells suspended in 100 μL PBS buffer per mouse) were injected subcutaneously into the right flanks of C57BL/6 mice. When the tumor volume reached about 100 mm^3, the LLC tumor-bearing mice were used for the in vivo experiments.

In vivo Fluorescence Imaging

The LLC tumor-bearing C57BL/6 mice were anesthetized with 5% isoflurane. Then, the mice were administrated with BITT and TB with a BITT dose of 1 mg/kg via intravenous injections, respectively (n=3). The in vivo fluorescence imaging was captured on the in vivo imaging system (PerkinElmer, USA) at different time points (1, 4, 8, 12, 24, and 48 h) after injection. To evaluate the tissue distribution of TB, the mice were sacrificed at 48 h postinjection. Tumors and major organs including heat, liver, spleen, lung, and kidney were harvested, followed by fluorescence imaging and quantitative analysis via the in vivo imaging system (PerkinElmer, USA). To investigate the pharmacokinetics of TB, the plasma was collected from the TB or BITT-treated mice after post-injection at different time points (0, 1, 2, 4, 6, 8, 12, and 24 h). The relative fluorescence intensity was also measured by the in vivo imaging system (PerkinElmer, USA). Mice with PBS treatment were chosen as the negative control.

In vivo Therapeutic Study

To evaluate the in vivo therapeutic efficacy of TB, the LLC tumor-bearing mice were randomly divided into five groups (n=4), followed by the treatments of PBS, PBS with laser irradiation (PBS+L), BITT, BITT with laser irradiation (BITT+L), and TB with laser irradiation (TB+L), respectively. For PBS and BITT groups, the LLC tumor-bearing mice were intravenously injected with PBS and BITT (1 mg/kg) without the subsequent laser irradiation, respectively. For PBS+L, BITT+L, and TB+L groups, the tumor-bearing mice were administrated with PBS, BITT, and TB (1 mg/kg BITT) via intravenous injections, respectively. At 12 h after administration, the tumor sites were exposed to laser irradiation (658 nm, 2 W·cm^{-2}) for 10 min. The treatments were carried out every three days during the 15-day study, and the tumor volume and body weight were both recorded. The tumor volume (V) was measured via a vernier caliper and calculated by the equation (1):

$$V = (a \times b2)/2 \tag{1}$$

Where V is the tumor volume, a is the tumor length and b is the tumor width.
The relative tumor volume (RTV) was calculated with the equation (2):

$$RTV = V/V0 \tag{2}$$

Where RTV is the relative tumor volume, V is the tumor volume and V0 is the initial tumor volume on day 0. The relative body weight (RBW) was calculated by the equation (3):

$$RBT = (W - W0)/W0 \quad (3)$$

Where RBT is the relative body weight, W is the body weight and W0 is the initial body weight on day 0.

Histological and Immunohistochemical Analysis

After the treatment of 15 days, mice after different treatments were euthanized. Blood samples of the treated mice were collected and tested for the hematology analysis. Then, the mice were sacrificed. The tumors and major organs (including hearts, livers, spleens, lungs, and kidneys) were collected and fixed in 4% formalin saline for 24 h. The fixed tissues were embedded in paraffin and sectioned at 5 μm thickness. The slices of tumors were stained with H&E, TUNEL, CD4, and CD8 staining, respectively. The stained slices were photographed by an inverted fluorescence microscope (Leica, Japan). For the in vivo biosafety evaluation, the collected major organs were also sectioned and stained with H&E analysis.

Statistical Analysis

Experiments were performed on at least three replicates. All the results were expressed as the mean standard deviation (SD). Statistical significance was analyzed by one-way analysis of variance (ANOVA) with a Tukey post-hoc test using SPSS 13.0 software. A *p*-value of less than 0.05 ($p < 0.05$) was considered statistically significant.

Results and Discussion

Synthesis and Characterization of BITT and TB

The preparation of TB was illustrated in Scheme 1. The BITT nanoparticles were prepared by the self-assembly method in deionized water, followed by the sonication of the nanoparticles in the suspension. For the T cell membrane coating on BITT, T cells were harvested from the spleens in mice. The collected T cells expressed high levels of CD8, CD45, and CD3 (Figure S1A–S1C in the supplementary materials file), which indicated that the $CD8^+$ T cells were successfully collected. After the induction with Phorbol-12-myristate-13-acetate and Ionomycin, PD-1 was detected to be highly expressed on the cell surface by flow cytometry (FACS) analysis (Figure S2 in the supplementary materials file), which was an important receptor on T cells for immune checkpoint therapy and served as a key targeting ligand for active tumor accumulation. The cell membranes were collected and used to camouflage BITT nanoparticles through sonication and physical extrusion. We investigated the physicochemical properties of BITT and TB. The transmission electron microscope (TEM) images indicated that both BITT and TB were uniform and spherical (Figure 1A and B). Dynamic light scattering (DLS) measurement indicated that BITT nanoparticles showed an average hydrodynamic diameter of 130.0 ± 1.7 nm with a PDI of 0.15, and the one of TB was 199.3 ± 4.1 nm with a PDI of 0.12, consistent with the TEM observations (Figure 1A and B). DLS measurement and TEM imaging demonstrated that the particle sizes of BITT and TB might be beneficial for improving the circulation lifetime with an appropriate size of less than 200 nm.[24] To confirm the $CD8^+$ T cell membrane decoration on BITT, the profiles of membrane proteins on TB were performed via sodium dodecyl sulfate-polyacrylamide gel electrophoresis (SDS-PAGE). The SDS-PAGE indicated that TB displayed a protein profile similar to those of T cell membranes and T cell lysate (Figure 1C). The data mentioned above demonstrated that TB was successfully prepared by coating BITT with $CD8^+$ T cell membranes.

We further analyzed the parameters, such as zeta potential, fluorescence/UV-Vis spectra, and thermal properties. Zeta potential analysis indicated that BITT was −15 mV and TB was −30 mV (Figure 1D), respectively, implying that the camouflage with T cell membranes induced a higher negative charge. The fluorescence spectra analysis indicated that BITT and TB in water displayed a maximum excitation wavelength at 534 nm and the fluorescence emission one at 730 nm (Figure 1E and F), implying that the camouflage with cell membranes did not change the fluorescent characteristics of BITT significantly. The Ultraviolet-visible spectroscopy (UV-Vis) analysis also indicated that the maximum absorption peak was at ~550 nm (Figure 1G). To investigate the photothermal conversion behavior of TB, the temperature changes were recorded under laser irradiation. The photothermal heating curves of TB in water revealed power density-dependent temperature variation behavior under the 658 nm laser irradiation (Figure 1H). The photothermal properties of BITT were also studied under 658 nm laser irradiation. The temperature of TB was significantly increased with the laser irradiation power density increased. When the irradiation power

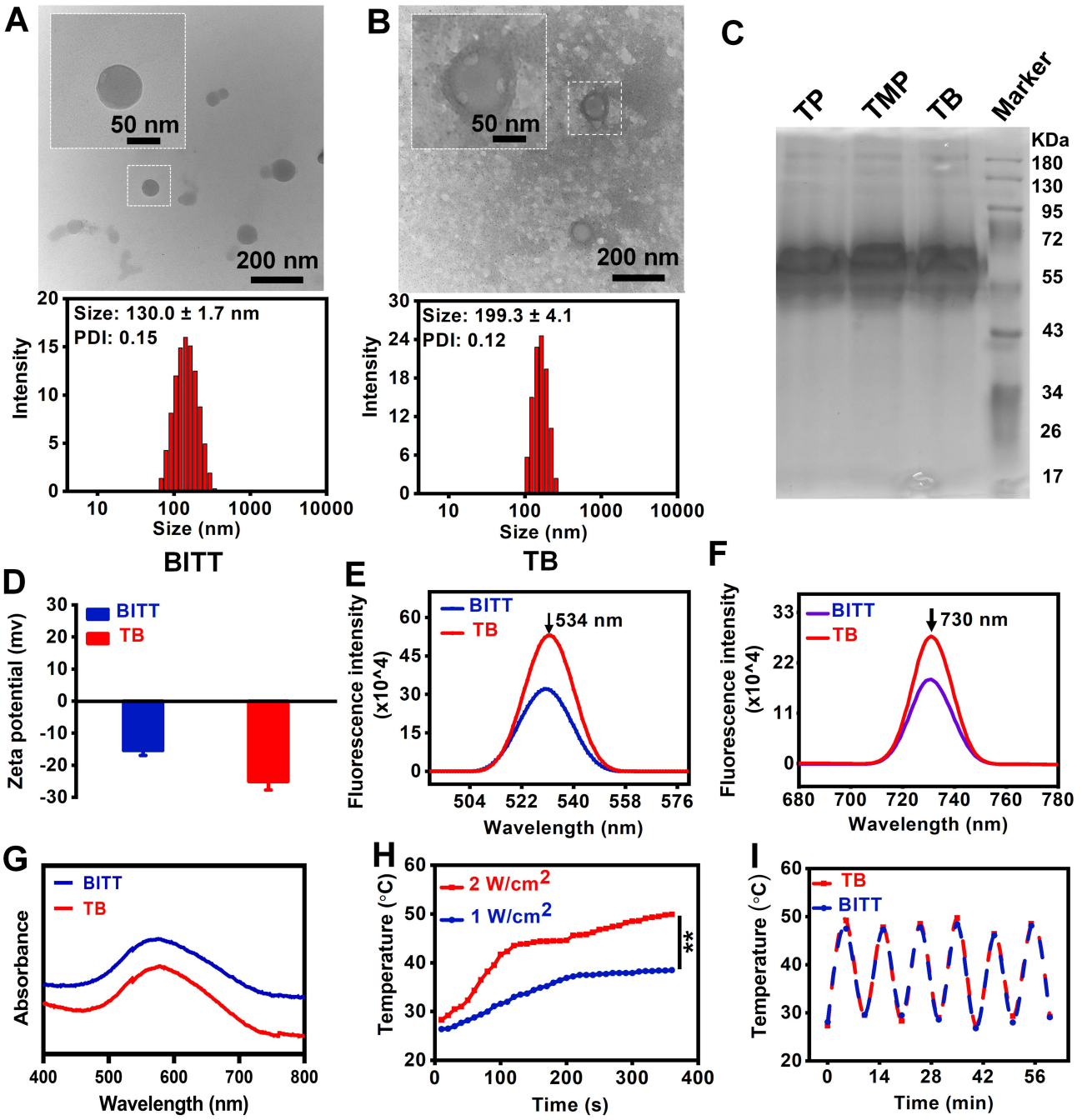

Figure 1 Characterization of the nanoparticles. (**A**) TEM and DLS analysis of BITT. (**B**) TEM and DLS analysis of TB. (**C**) SDS-PAGE analysis of T cell proteins (TP), T cell membrane (TMP), and TB. (**D**) Zeta potential of BITT and TB. (**E**) Excitation spectra of BITT and TB with an emission wavelength of 730 nm (20 μg·mL^{-1} BITT). (**F**) Emission spectra of BITT and TB with an excitation wavelength of 658 nm (20 μg·mL^{-1} BITT). (**G**) UV absorption spectra of BITT and TB (20 μg·mL^{-1} BITT). (**H**) Photothermal effect of TB under 658 nm laser irradiation with a powder density of 1 or 2 W·cm^{-2}, respectively. (**I**) Photothermal stability of BITT and TB (20 μg·mL^{-1} BITT) under laser irradiation (658 nm, 2 W·cm^{-2}) during 6 cycles of heating and natural cooling processes.

density was 2 W·cm^{-2}, the temperature of TB reached 50°C after irradiation for 5 min. At the same time, to further evaluate the photodynamic performance of TB nanoparticles in solution, we used SOSG probe to monitor the changes in BITT before and after light irradiation (Figure S3 in the supplementary materials file). The result showed that, compared with the control group, both the TB+L and BITT+L groups exhibited significantly enhanced SOSG fluorescence, indicating efficient singlet oxygen generation. This suggests that the photodynamic performance of TB nanoparticles in solution remains unaffected. The photothermal stability of TB was also investigated. Under a 658 nm laser irradiation (2 W·cm^{-2}), the maximum solution temperatures

of BITT and TB (20 μg·mL^{-1} BITT) showed no obvious change during the 6 cycles of the natural cooling process, suggesting the excellent photostability of both BITT and TB (Figure 1I). The parameters indicated that TB might be useful in phototherapy. To eliminate the influence of TB solution on the photodynamic performance, we used a thermal infrared imager to test the different components containing BITT (Figure S4 in the supplementary materials file). From the result, it can be seen that except for the BITT group, the other control groups did not show any temperature changes whether in the presence or absence of irradiation. That indicated that the temperature increase of the TB nanoparticles was caused by BITT rather than the solvent.

The results indicated that the T cell membrane coating did not affect the excellent optical performance of BITT. For example, TB showed excellent light-to-heat conversion ability and photothermal stability after a 658 nm laser irradiation, which might be applied to tumor photothermal therapy. All these characteristics demonstrated that we successfully prepared TB, which might be useful in the treatment of lung cancer.

The Binding to LLC Cells

We evaluated the binding to the cells in vitro by the nanoparticles. To investigate the binding, confocal laser microscopy (CLSM) and flow cytometry (FACS) analysis was performed. The BITT-positive cells displayed a BITT concentration and time-dependent manner (Figure 2A and B). FACS analysis showed that when the concentration of BITT increased to 20 μg·mL^{-1}, the BITT-positive LLC cells were up to 93.6% after 6 h incubation, which was a 15-fold increase compared with those in low concentration (BITT, 5 μg·mL^{-1}) (Figure 2A). TB bound to LLC cells within 1 h, and stronger fluorescence could be observed with the incubation time extended (Figure 2B). The BITT-positive cells were increased to 92.4% with the incubation time extended to 9 h. Moreover, the fluorescence intensity of TB was stronger than that of the negative control and BITT group (Figure S5 in the supplementary materials file). The data indicated TB showed a high-level binding efficiency in the optimized conditions including the dosage of 20 μg·mL^{-1} and incubation for 9 h with TB, which was used for further experiments. TB exhibited excellent specific binding ability to LLC cells in vitro, which might be due to the interactions between the overexpressed PD-1 receptors on TB and the overexpressed PD-L1 ligand on LLC cells (Figure S6 in the supplementary materials file). To verify that the binding of PD-1/PD-L1 effectively promotes the uptake of BITT by LLC cells, we treated the LLC cells with the PD-L1 inhibitor (Figure S7 in the supplementary materials file). From the result, the fluorescence intensity of the TB group with the inhibitor was similar to that of the BITT group. Clearly, the TB group had the strongest fluorescence due to the mutual binding of PD-1 and PD-L1. CLSM and FACS analysis demonstrated that TB bound to LLC cells effectively. The in vitro phototherapeutic effect of TB will be further evaluated.

In vitro Phototherapy Effects

As an AIEgen-base photosensitizer, TB was supposed to show excellent photothermal capacity and efficient intercellular ROS generation ability for cancer therapy. ROS generation induced by AIEgen-base photosensitizer might play an important role in cancer cell inhibition. The intracellular ROS generation of TB was evaluated by DCFH-DA as an indicator. LLC cells treated with BITT and TB displayed a strong green fluorescence signal upon 658 nm laser irradiation for 5 min, but no obvious green fluorescence signal was observed in the negative controls (PBS, PBS+L, or BITT without laser irradiation) (Figure 3C). These phenomena demonstrated that both BITT and TB with laser irradiation aroused intracellular ROS generation efficiently. The green fluorescence signal of TB was significantly stronger than that of BITT, indicating that the $CD8^+$ T cell membrane coating might enhance the intracellular ROS generation of TB.

The Live/Dead assay was also carried out by Calcein-AM/Propidium Iodide (PI) staining to differentiate live (green) and dead (red) cells. As illustrated in Figure 3A, the strong green fluorescence was found in laser irradiation or BITT without laser irradiation group. However, the strong red one was observed in cells with BITT or TB with laser irradiation, which indicated that BITT or TB with laser irradiation could induce the death of lung cancer cells effectively. Compared to BITT, the red fluorescence intensity of TB was significantly stronger, which indicated that TB exhibited enhanced tumor inhibition by the coating with $CD8^+$ T cell membranes.

To evaluate the in vitro cell inhibition, the Cell counting kit-8 (CCK-8) assay was performed by the treatment with TB with or without laser irradiation on LLC cells. As shown in Figure 3B, the cell viabilities of LLC cells were retained up to 90% for 48 h, with BITT concentrations ranging from 0 to 40 μg/mL, indicating the good biocompatibility of TB. After the exposure to 658 nm laser irradiation, the cell viabilities of LLC cells were gradually decreased with BITT

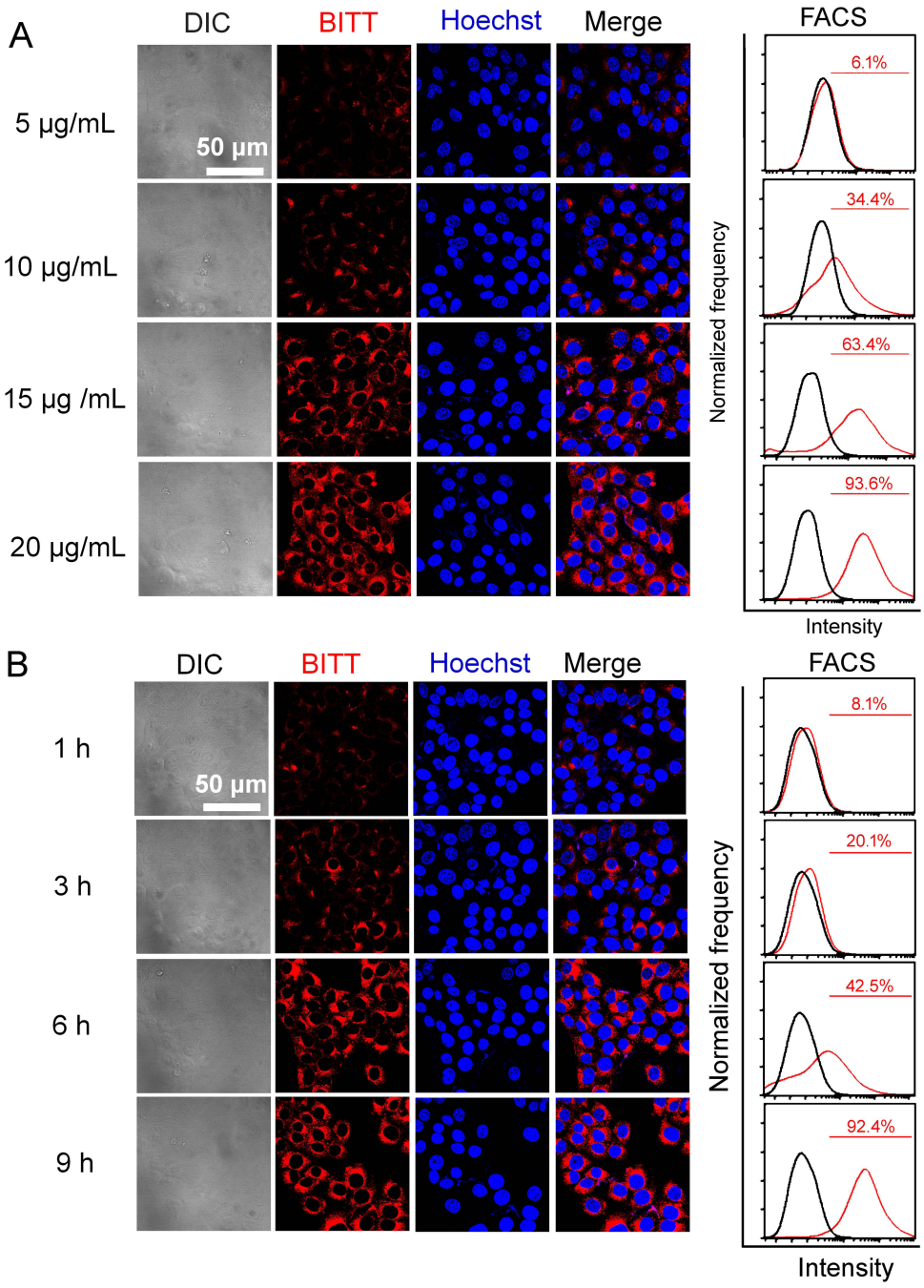

Figure 2 The binding efficiency of TB to LLC cells. (**A**) CLSM and FACS analysis of LLC cells treated with TB at various BITT concentrations for 6 h. LLC cells were treated with TB at various BITT concentrations (5, 10, 15, and 20 μg·mL^{-1}) for 6 h. (**B**) CLSM and FACS analysis of LLC cells treated with TB for 1, 3, 6, and 9 h, respectively. For CLSM analysis, the cells were stained with Actin-488 (green), and the nuclei were stained with Hoechst (blue). The cells without any treatment were chosen as the negative control (NC).

concentration increased, which was lower than 10% with BITT increasing to 20 μg/mL. The CCK-8 results indicated that TB led to effective cell death in the presence of laser irradiation, which demonstrated that TB showed excellent cell inhibition effect in the presence of laser irradiation.

To evaluate the potential tumor inhibition, the three-dimensional (3D) tumor spheroid models generated with LLC cells were constructed to evaluate the penetration ability and the phototherapeutic effect of TB in vitro. The 3D tumor spheroid of LLC cells treated with different formulations was also stained by Calcein-AM/PI assay. CLSM analysis indicated that the 3D tumor spheroids showed significant red fluorescence after the treatment with BITT upon laser irradiation (Figure 3D),

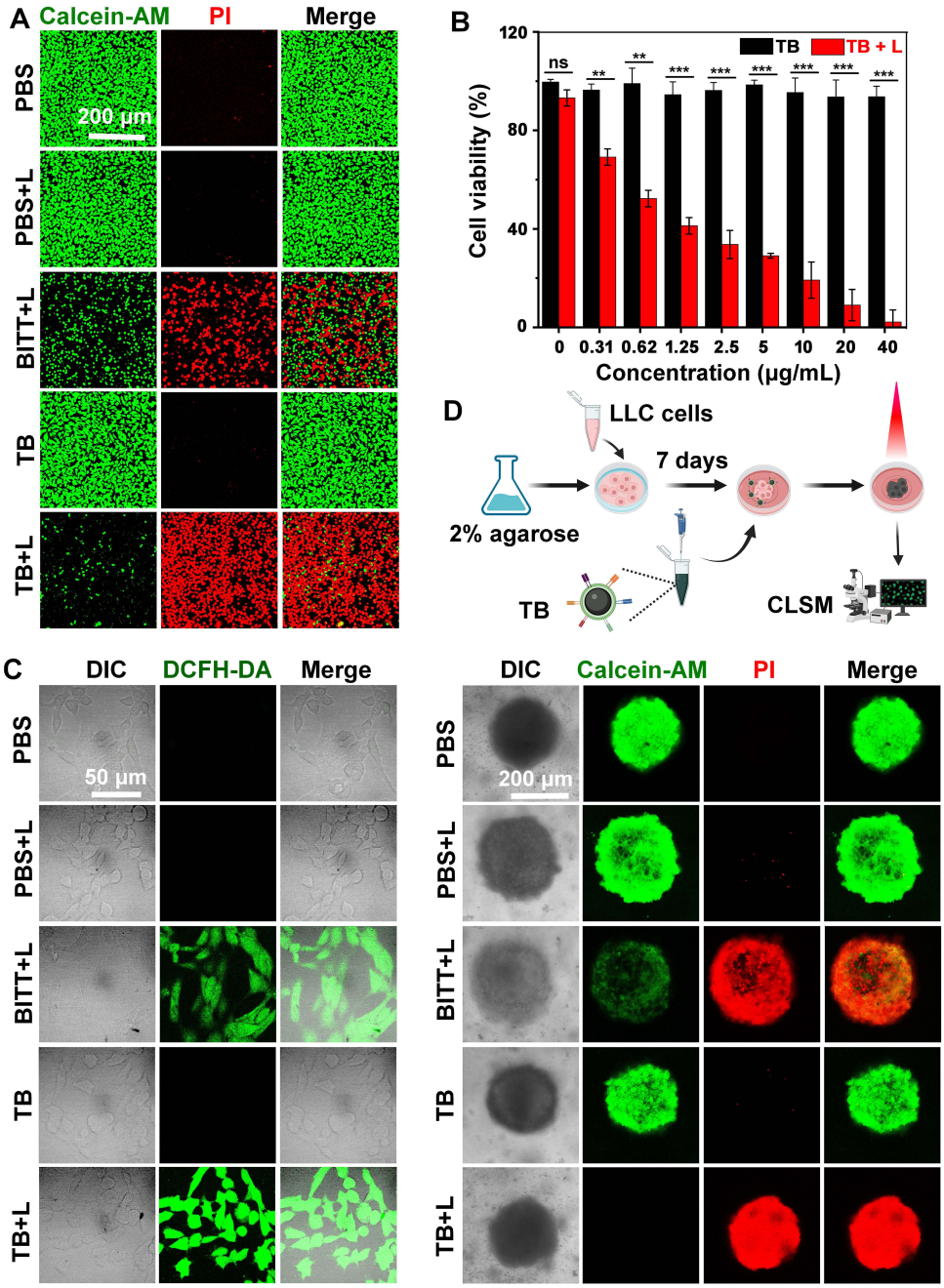

Figure 3 In vitro phototherapeutic effects on LLC cells treated with different formulations. (**A**) Live/dead assay of LLC cells by Calcein-AM/PI staining after different treatments. (**B**) Cell viability of LLC cells measured by CCK-8 method after treatment with different BITT concentrations with or without laser irradiation. (**C**) Intracellular ROS level in LLC cells indicated by DCFH-DA after different treatments. (**D**) Live/Dead assay of LLC 3D tumor spheroid stained by Calcein-AM/PI after different treatments. The laser irradiation was performed in the parameters including 658 nm, 2 W·cm^{-2}, and 300 s). Scanning images of the LLC 3D tumor spheroid by CLSM were shown at the depth from 68 μm to 101 μm. For A and D, the live and dead cells were distinguished with Calcein-AM/ PI. ***P*<0.01; ****P*<0.001; ns, no significant differences.

implying that most of the cancer cells were dead with PI as an indicator. By contrast, the green fluorescence but without an obvious red fluorescence signal could be found in the spheroids treated with the control groups including PBS, PBS plus Laser irradiation, and BITT, which meant that most of the cancer cells were alive. The results indicated that after the AIEgens (BITT and TB) penetrated the LLC 3D tumor spheroids, cell death was achieved in the presence of laser irradiation. Moreover, TB improved the penetration and phototherapeutic effects within the LLC 3D tumor spheroids compared to BITT (Figure 3D), which might be beneficial from the $CD8^+$ T cell membrane coating. The in vitro 3D tumor spheroid study indicated that TB with laser irradiation might show great potential in lung cancer therapy.

https://doi.org/10.2147/IJN.S536484

The results showed that TB enhanced tumor accumulation and promoted cell inhibition in the presence of laser irradiation, which might be attributed to the good tumor-targeting ability via the $CD8^+$ T membrane coating and BITT-induced efficient intercellular ROS generation and photothermal effect. Thus, TB exhibited excellent phototherapeutic effect on lung cancer cells in vitro, which might be useful for the in vivo application of tumor phototherapy.

In vivo Tracking

To evaluate the phototherapy, the tumor accumulation and circulation properties of the nanodrugs are critical parameters. We investigated the above factors of TB in LLC-tumor-bearing mice. As illustrated in Figure 4A, significant fluorescence signals were captured on tumor sites after the intravenous injection of TB for 1 h. Then, the fluorescence intensity in the tumor area was gradually increased and reached the highest level at 8 h post-injection, implying that TB could be efficiently accumulated in the tumors. Compared with TB, BITT showed much less fluorescence in tumor sites. The results implied that TB exhibited much higher tumor accumulation than BITT, which might be ascribed to the active tumor targeting ability via $CD8^+$ T cell membrane coating. Notably, the fluorescence intensity of BITT was significantly decreased after 12 h, implying that the clearance of the AIEgens from the body. However, the fluorescence intensity remained higher in TB than in BITT at 48 h post-injection, which might be attributed to the strong binding through the interactions between PD-1 on the $CD8^+$ T cell membrane and PD-L1 on the lung cancer cells. The fluorescence images and semi-quantitative fluorescence intensity of the ex vivo organs from mice were detected in Figure 4B and C. The fluorescence intensity of the tumors treated with TB was 2-fold higher than those treated with BITT ($P<0.001$), which was consistent with the in vivo fluorescence imaging. Obviously, TB also showed significant accumulation in the liver and lungs. Nanoparticles accumulate highly in the liver primarily due to its rich blood supply, filtration function, and efficient capture by Kupffer cells (liver macrophages) of the reticuloendothelial system (RES). In the lungs, high accumulation occurs because of their dense capillary network trapping particles, initial distribution after intravenous injection or inhalation, and active uptake by alveolar macrophages.[35,36] The results demonstrated that TB showed enhanced accumulation on the tumors and excellent fluorescence for in vivo imaging, which might contribute to good phototherapeutic effect and real-time tracking.

The pharmacokinetic behavior of TB was also evaluated in healthy mice to investigate the circulation lifetime of TB. The results indicated that the half-time ($T_{1/2}$) of TB in blood was approximately 8 h, which was 1.6 times longer than that of BITT ($T_{1/2}$ of BITT: ~5 h, $P<0.05$) (Figure S8 in the supplementary materials file). Similarly, the corresponding pharmacokinetic studies demonstrated that TB effectively enhanced the long circulation after $CD8^+$ T cell membrane decoration. It might be implied that both the favorable particle size of BITT and the coating with $CD8^+$ T cell membrane improved the circulation lifetime significantly, which was beneficial for the accumulation of the tumors.

The in vivo tracking and pharmacokinetic indicated that TB could accumulate in the tumor sites effectively and show good performance on the imaging. Based on the camouflage with $CD8^+$ T cell membranes, TB was endowed with an active targeting effect and binding to tumor tissues effectively. Furthermore, the good performance of AIEgens facilitated the real-time detection of the biodistribution of nanoparticles. Thus, TB could be quite beneficial to the in vivo phototherapy for lung cancer.

In vivo Therapeutic Effects

To evaluate the in vivo therapeutic effect of TB, the antitumor effects were investigated on LLC tumor-bearing mice (Figure 5A). The thermal imaging analysis indicated that the treatment with TB showed a temperature of 58.7°C in the presence of 658 nm laser irradiation (2 $W \cdot cm^{-2}$) for 10 min (Figure S9 in the supplementary materials file). In contrast, the treatment with TB only induced a temperature of 38.5°C without laser irradiation. The treatment with BITT induced a temperature of 47.2°C in the presence of laser irradiation, implying a weaker thermal effect, compared with the TB-treated ones. Correspondingly, the tumor growth curves showed that TB with the laser irradiation exhibited the strongest antitumor effect in all the treatment groups ($P<0.05$ vs BITT+L, $P<0.001$ vs the negative controls) (Figure 5B), which was consistent with the extracted tumors (Figure 5D). However, the relative tumor volumes were increased gradually and showed no significant difference ($P>0.05$) in all control groups (PBS, PBS with laser irradiation, and BITT without irradiation) (Figure 5D). Although BITT with laser irradiation showed some tumor inhibition compared with the single BITT treatment

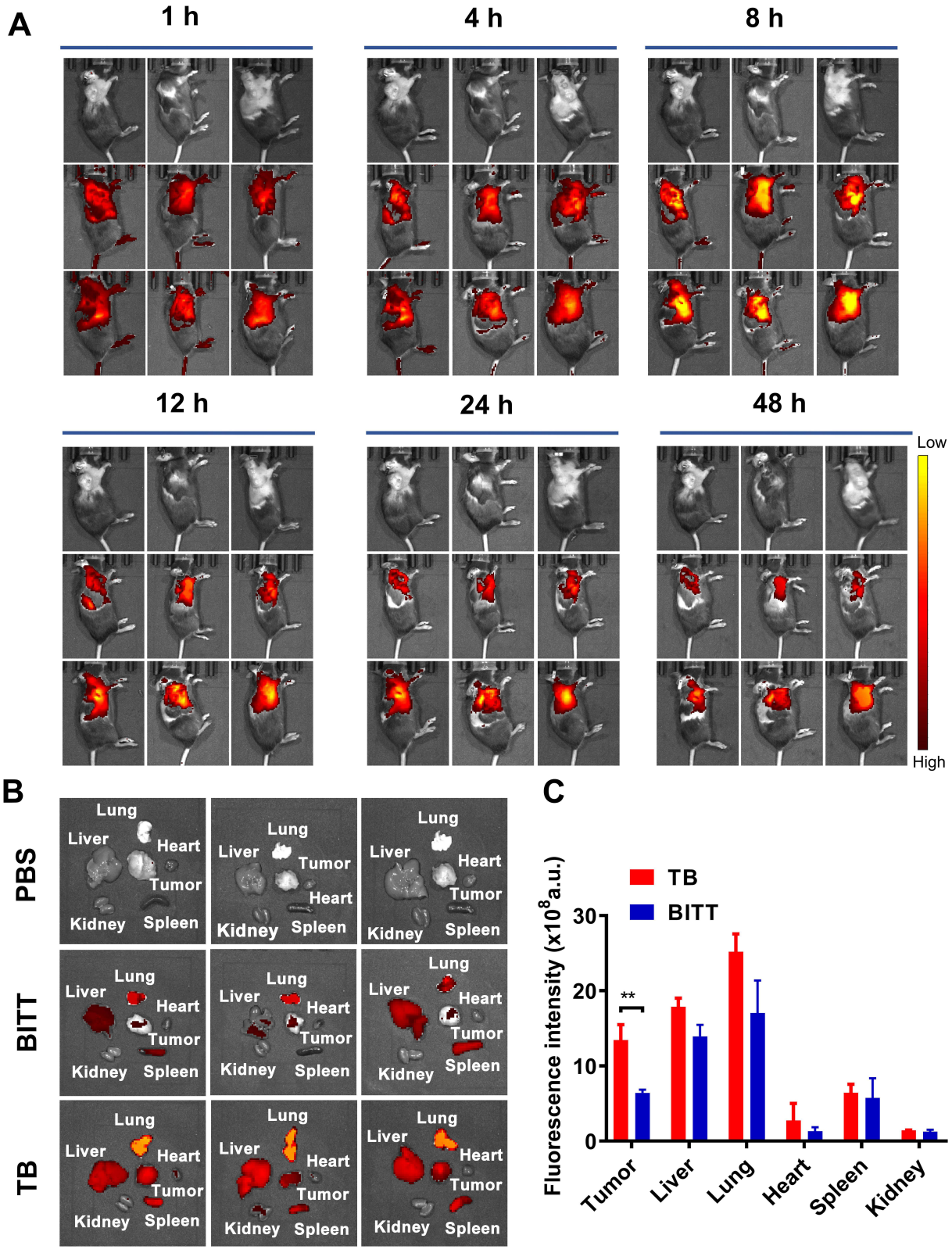

Figure 4 In vivo imaging of TB on mice bearing xenograft LLC tumors. (**A**) Fluorescence images of LLC tumor-bearing mice at different time points (1, 4, 8, 12, 24, and 48 h) after intravenous injection of BITT and TB (BITT: 1 mg/kg). Mice treated with PBS were chosen as the negative control. (**B**) Fluorescence images of ex vivo organs on mice at 48 h after intravenous injection of TB and BITT (BITT: 1 mg/kg). Mice treated with PBS were chosen as the negative control. (**C**) Fluorescence intensity of ex vivo tissues on mice at 48 h after intravenous injection of TB and BITT (BITT: 1 mg/kg). $^{**}P<0.01$.

https://doi.org/10.2147/IJN.S536484

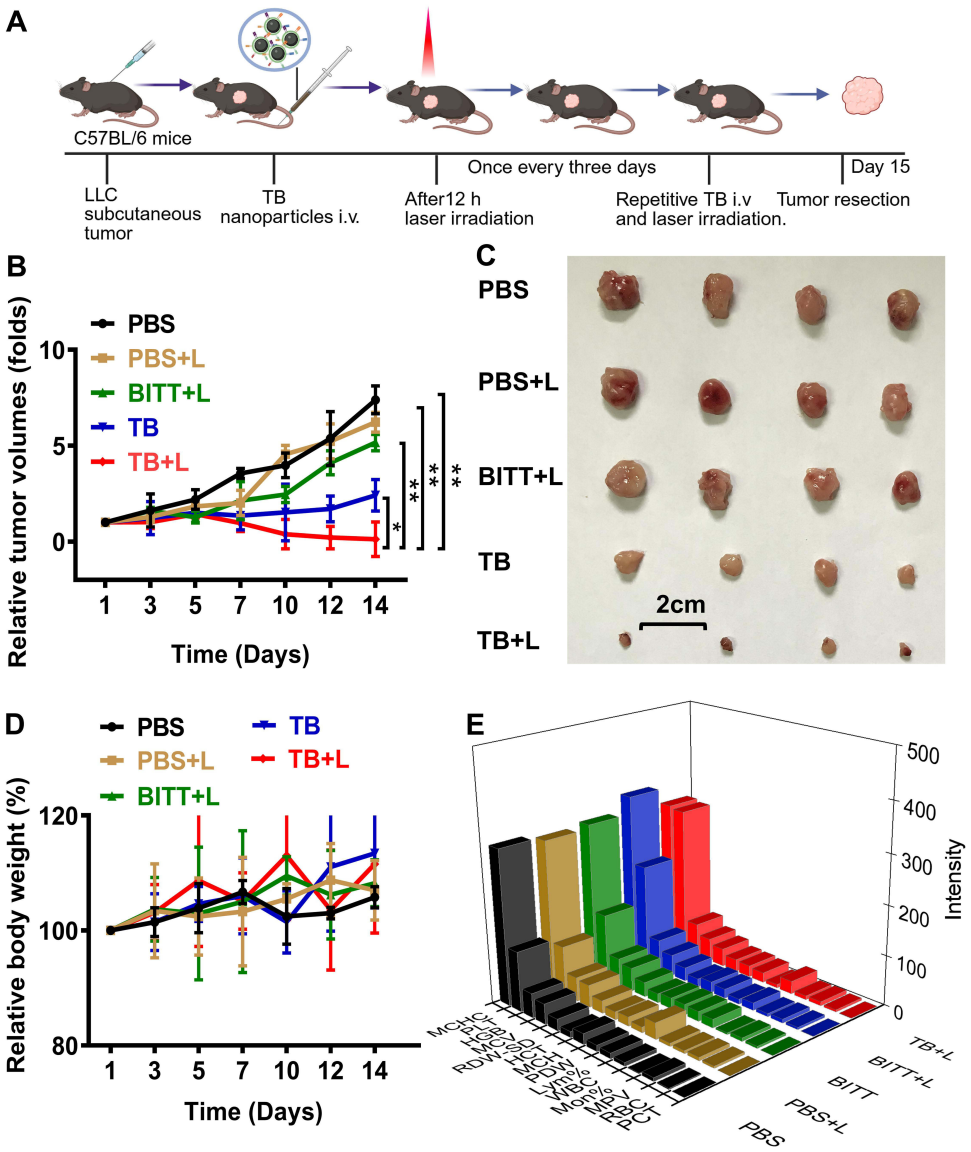

Figure 5 In vivo therapeutic efficacy of TB on LLC tumor-bearing mice. (**A**) Experimental timeline for in vivo study. (**B**) Tumor growth curves of LLC tumor-bearing mice after different treatments. (**C**) Photograph of tumors extracted from mice on day 14 after different treatments (BITT: 1 mg/kg). (**D**) Body weight changes of LLC tumor-bearing mice after different treatments. (BITT: 1 mg/kg). (**E**) Blood routine assay of LLC tumor-bearing mice on day 14 after various treatments. *P<0.05; **P<0.01.

(P<0.001), the tumor inhibition was much lower than the one of TB with laser irradiation (Figure 5B and C). The effective tumor inhibition induced by TB with laser irradiation indicated that not only the favorable nanostructure and aggregated-induced emission properties but also the $CD8^+$ T cell membrane coating promoted the phototherapeutic effects.

Biosafety is an important precondition for lung cancer therapy. We examined the body weight every other day. The relative body weight showed no significant changes in all of the administration (P>0.05) (Figure 5D), indicating that no obvious side effects were found after different treatments. After the treatment for 14 days, the blood from mice was collected for the blood routine assay, which also indicated that the routine blood indexes in all the treatment groups were presented in the normal range, implying that no apparent systemic toxicity of TB with laser irradiation treatment (Figure 5E). Hematoxylin and eosin (H&E) staining images of the major organs (including heart, liver, lung, spleen, and kidney) also showed that TB with laser irradiation had no obvious organ damages or inflammatory lesions compared with the other treatments (Figure 6A), further revealing the good biocompatibility and biosafety of TB.

T cell activation plays an important role in lung cancer immunotherapy. The activation of $CD4^+$ and $CD8^+$ T cells in tumors potentially remodeled the tumor microenvironment to overcome tumor-associated immune suppression, which

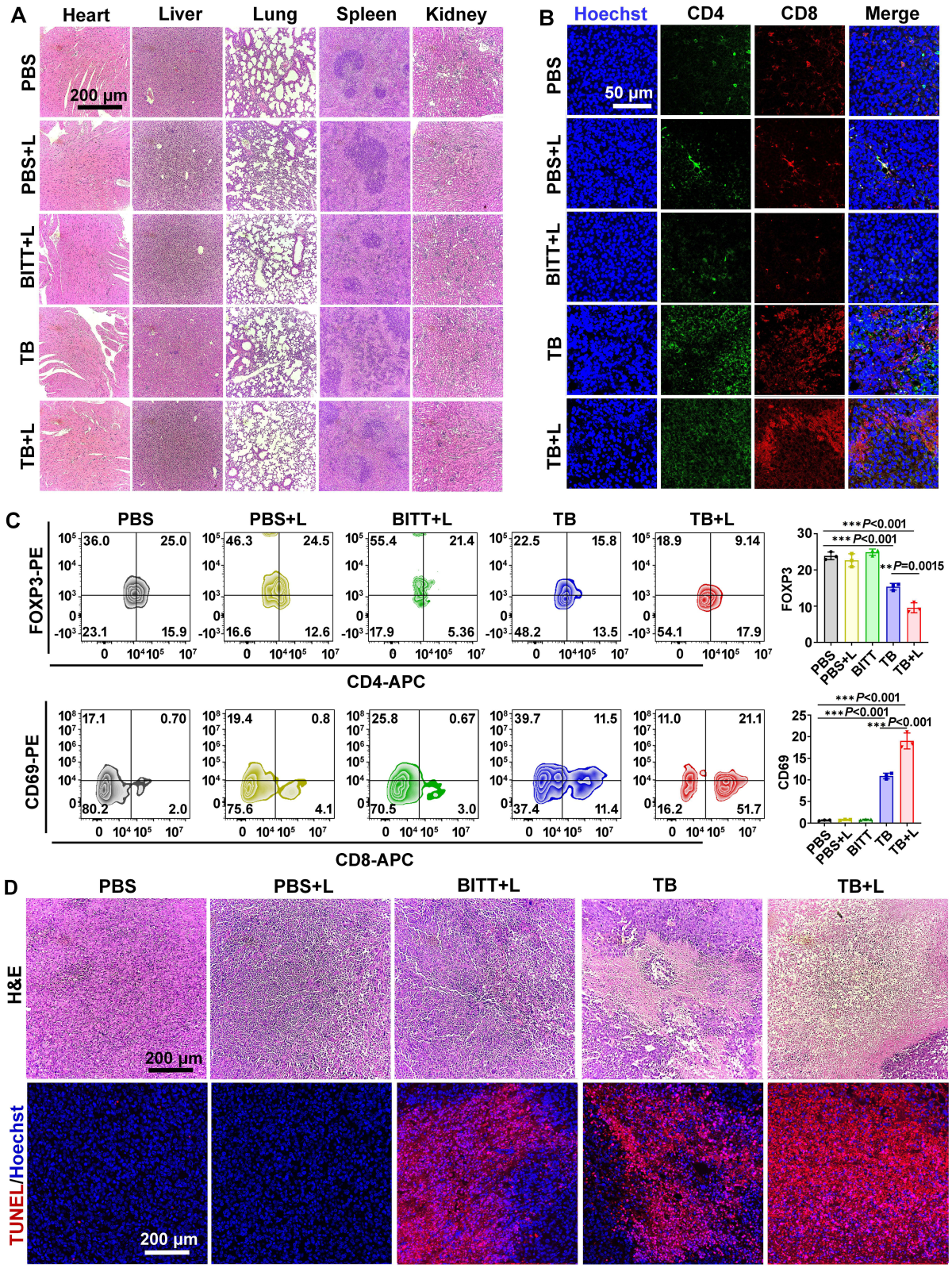

Figure 6 Histological staining analysis after different treatments. (**A**) H&E staining images of major organ sections from LLC tumor-bearing mice on the 14th day of treatment. (**B**) CD4 (green) and CD8 (red) staining analysis of tumor sections from LLC tumor-bearing mice on the 14th day of treatment. (BITT: 1 mg/kg). (**C**) FACS analysis of the infiltration of T cells. (**D**) H&E and TUNEL (red) staining analysis of tumor sections from LLC tumor-bearing mice on the 14th day of treatment (BITT: 1 mg/kg). The nucleus was stained with Hoechst (blue). $^{**}P<0.01$; $^{***}P<0.001$.

https://doi.org/10.2147/IJN.S536484

provided a promising strategy to enhance immunotherapy for lung cancer. Herein, the novel AIEgen TB camouflaged with $CD8^+$ T cell membranes, not only endowed the improved accumulation by the active targeting to LLC cells by the interactions between PD-1 and PD-L1 but facilitated the immunotherapy by the activations of T cells for lung cancer. To validate the therapeutic effects of TB, the tumors were harvested on day 14 after different treatments and then evaluated with H&E, TdT-mediated dUTP Nick-End Labeling (TUNEL), and immunofluorescence staining. As expected, the immunofluorescence staining in Figure 6B showed that significant fluorescence was found in BITT and TB with laser irradiation, which indicated that AIEgens with laser irradiation increased the levels of $CD4^+$ and $CD8^+$ T cells. Moreover, TB with laser irradiation exhibited stronger fluorescence compared to BITT in the presence of laser irradiation. FACS analysis indicated that the treatment with TB with laser irradiations reduced the populations of Treg cells and increased the activation of $CD8^+$ T cells, as was represented by the reduction of FOXP3 and CD4 signals and increase of CD69 and CD8 ones (Figure 6C). These results demonstrated that TB amplified the T cell response by the camouflage with T cell membranes. Meanwhile, H&E staining showed that the treatment with TB and laser irradiation induced significant tumor suppression with severe tumor cell necrosis or apoptosis (Figure 6D). Consistently, the TUNEL staining showed that the enhanced apoptosis of cancer cells represented by the red fluorescence in the group of TB with laser irradiation, which confirmed that TB induced the most effective apoptosis of cancer cells in the presence of laser irradiation. These results convincingly demonstrated that TB could facilitate synergistic tumor inhibition by excellent immunotherapy and phototherapeutic effects, which opened a new avenue for lung cancer therapy.

Conclusion

In conclusion, a type of biomimetic AIE aggregation (TB) was rationally designed and successfully fabricated. The prepared TB possessed improved binding efficiency, photothermal effects, and ROS generation ability to kill the lung cancer cells. Moreover, TB also showed improved circulation lifetime and excellent tumor targeting ability, which induced effective phototherapy and immunotherapy in vivo based on BITT and the $CD8^+$ T cell-derived membranes. The work provided a new perspective on the design of biomimetic AIEgens and offered an encouraging strategy for precise lung cancer therapy. However, future studies should investigate the effects of this nanoplatform on memory T cell subsets, including central memory T cells, to assess long-term immunotherapeutic efficacy. The clinical translation still faces challenges requiring further investigation, such as stability and storage conditions, biocompatibility, and toxicology profiles in human systems.

Acknowledgments

This work was financially supported by National Natural Science Foundation of China (82072047, 81370299, and 32171312), Major Project of Guangzhou National Laboratory (GZNL2024A01013), Medical Scientific Research Foundation of Guangdong Province (A2023047), the Guangzhou Science and Technology Project (2024A03J0891, 202201011593, and SL2022A03J00613), Plan on enhancing scientific research in GMU (2025SRP003 and 02-410-2302068XM), The Open research funds from The Sixth Affiliated Hospital of Guangzhou Medical University, Qingyuan Peoples Hospital (202201-303 and 202301-304).

Disclosure

The authors report no conflicts of interest in this work.

References

1. Siegel RL, Giaquinto AN, Jemal A. Cancer statistics, 2024. *CA Cancer J Clin*. 2024;74(1):12–49. doi:10.3322/caac.21820
2. Zhang L, Lin Y, Li S, et al. In situ reprogramming of tumor-associated macrophages with internally and externally engineered exosomes. *Angew Chem Int Ed*. 2023;62(11):e202217089. doi:10.1002/anie.202217089
3. Leiter A, Veluswamy RR, Wisnivesky JP. The global burden of lung cancer: current status and future trends. *Nat Rev Clin Oncol*. 2023;20(9):624–639. doi:10.1038/s41571-023-00798-3
4. Niu Z, Jin R, Zhang Y, et al. Signaling pathways and targeted therapies in lung squamous cell carcinoma: mechanisms and clinical trials. *Signal Transduct Target Ther*. 2022;7(1):353. doi:10.1038/s41392-022-01200-x
5. Overchuk M, Weersink RA, Wilson BC, et al. Photodynamic and photothermal therapies: synergy opportunities for nanomedicine. *ACS Nano*. 2023;17(9):7979–8003. doi:10.1021/acsnano.3c00891

6. Luo H, Gao S. Recent advances in fluorescence imaging-guided photothermal therapy and photodynamic therapy for cancer: from near-infrared-I to near-infrared-II. *J Control Release*. 2023;362:425–445. doi:10.1016/j.jconrel.2023.08.056
7. Xie Z, Fan T, An J, et al. Emerging combination strategies with phototherapy in cancer nanomedicine. *Chem Soc Rev*. 2020;49(22):8065–8087. doi:10.1039/D0CS00215A
8. Zhang Z, Du Y, Shi X, et al. NIR-II light in clinical oncology: opportunities and challenges. *Nat Rev Clin Oncol*. 2024;21(6):449–467. doi:10.1038/s41571-024-00892-0
9. Chen T, Yao T, Peng H, et al. An Injectable Hydrogel for simultaneous photothermal therapy and photodynamic therapy with ultrahigh efficiency based on carbon dots and modified cellulose nanocrystals. *Adv Funct Mater*. 2021;31(45):2106079. doi:10.1002/adfm.202106079
10. Qian J, Tang BZ. AIE luminogens for bioimaging and theranostics: from organelles to animals. *Chem*. 2017;3(1):56–91. doi:10.1016/j.chempr.2017.05.010
11. Wang Y, Nie J, Fang W, et al. Sugar-based aggregation-induced emission luminogens: design, structures, and applications. *Chem Rev*. 2020;120(10):4534–4577. doi:10.1021/acs.chemrev.9b00814
12. Zhao Z, Zhang H, Tang BZ, et al. Aggregation-induced emission: new vistas at the aggregate level. *Angew Chem Int Ed*. 2020;59(25):9888–9907. doi:10.1002/anie.201916729
13. Kang M, Zhang Z, Chen X, et al. Aggregation-enhanced theranostics: AIE sparkles in biomedical field. *Aggregate*. 2020;1(1):80–106. doi:10.1002/agt2.7
14. Cen P, Huang J, Zhang H, et al. Aggregation-induced emission luminogens for in vivo molecular imaging and theranostics in cancer. *Aggregate*. 2023;4(5):e352. doi:10.1002/agt2.352
15. Feng X, Tong B, Dong Y, et al. Recent progress of aggregation-induced emission luminogens (AIEgens) for bacterial detection and theranostics. *Mater Chem Front*. 2021;5(3):1164–1184. doi:10.1039/D0QM00753F
16. Zhang L, Wang Z, Zhao Y, et al. Multi-stimuli-responsive and cell membrane camouflaged aggregation-induced emission nanogels for precise chemo-photothermal synergistic therapy of tumors. *ACS Nano*. 2023;17(24):25205–25221. doi:10.1021/acsnano.3c08409
17. Zhu W, Kang M, Li C, et al. Zwitterionic AIEgens: rational molecular design for NIR-II fluorescence imaging-guided synergistic phototherapy. *Adv Funct Mater*. 2021;31(3):2007026. doi:10.1002/adfm.202007026
18. Ding K, Wang L, Zhang W, et al. Photo-enhanced chemotherapy performance in bladder cancer treatment via albumin coated AIE aggregates. *ACS Nano*. 2022;16(5):7535–7546. doi:10.1021/acsnano.1c10770
19. Lin Y, Yi M, Li S, et al. "Two birds with one stone" strategy for the lung cancer therapy with bioinspired AIE aggregates. *J Nanobiotechnol*. 2023;21(1):49. doi:10.1186/s12951-023-01799-1
20. Fang RH, Kroll AV, Zhang L, et al. Cell membrane coating nanotechnology. *Adv Mater*. 2018;30(23):1706759. doi:10.1002/adma.201706759
21. Celadon A, Sun H, Zhang G, et al. Batteries for electric vehicles: technical advancements, environmental challenges, and market perspectives. *SusMat*. 2024;4(5):e234. doi:10.1002/sus2.234
22. Li H, Li S, Huang X, et al. Artificial exosomes mediated spatiotemporal-resolved and targeted delivery of epigenetic inhibitors. *J Nanobiotechnol*. 2021;19(1):364. doi:10.1186/s12951-021-01107-9
23. Liang L, Cen H, Wang S, et al. The reversion of DNA methylation-induced miRNA silence via biomimetic nanoparticles-mediated gene delivery for efficient lung adenocarcinoma therapy. *Mol Cancer*. 2022;21(1):186. doi:10.1186/s12943-022-01651-4
24. Zhang Y, Yang L, Chen S, et al. Bioinspired metal–organic frameworks mediated efficient delivery of siRNA for cancer therapy. *Chem Engin J*. 2021;426:131926. doi:10.1016/j.cej.2021.131926
25. Yang L, Lin Y, Miao Y, et al. Biomimetic metal–organic frameworks navigated biological bombs for efficient lung cancer therapy. *J Colloid Interf Sci*. 2022;625:532–543. doi:10.1016/j.jcis.2022.06.008
26. Gu X, Wei H, Chen L, et al. Itaconate promotes hepatocellular carcinoma progression by epigenetic induction of $CD8^+$ T-cell exhaustion. *Nat Commun*. 2023;14(1):8154. doi:10.1038/s41467-023-43988-4
27. Lv Z, Li Z, Zhang R, et al. A smart DNA nanoassembly containing multivalent aptamers enables controlled delivery of CRISPR/Cas9 for cancer immunotherapy. *Adv Funct Mater*. 2024;34(12):2311069. doi:10.1002/adfm.202311069
28. Lin YX, Wang Y, Yu M, et al. Reactivation of the tumor suppressor PTEN by mRNA nanoparticles enhances antitumor immunity in preclinical models. *Sci Transl Med*. 2021;13(599):eaba9772. doi:10.1126/scitranslmed.aba9772
29. Luo Z, He T, Liang X, et al. Self-adjuvanted molecular activator (SeaMac) nanovaccines promote cancer immunotherapy. *Adv Healthc Mater*. 2021;10(7):2002080. doi:10.1002/adhm.202002080
30. Liu L, Pan Y, Rao L, et al. Boosting checkpoint immunotherapy with biomaterials. *ACS Nano*. 2023;17(4):3225–3258. doi:10.1021/acsnano.2c11691
31. Zhang Y, Qin Y, Yang L, et al. Artificial platelets for efficient siRNA delivery to clear "Bad Cholesterol". *ACS Appl Mater Interfaces*. 2020;12(25):28034–28046. doi:10.1021/acsami.0c07559
32. Zhang HT, Peng R, Tang W, et al. Versatile nano-PROTAC-induced epigenetic reader degradation for efficient lung cancer therapy. *Adv Sci*. 2022;9(29):2202039. doi:10.1002/advs.202202039
33. Chi SY, Zuo MM, Liu ZH, et al. Loading drugs in natural phospholipid bilayers of cell membrane shells to construct biomimetic nanocomposites for enhanced tumor therapy. *ACS Appl Mater Interfaces*. 2022;14(25):28671–28682. doi:10.1021/acsami.2c08587
34. Märkl S, Schroter A, Hirsch T. Small and bright water-protected upconversion nanoparticles with long-time stability in complex, aqueous media by phospholipid membrane coating. *Nano Lett*. 2020;20(12):8620–8625. doi:10.1021/acs.nanolett.0c03327
35. Zhang D, Lin ZG, Liu XL. Ultrasound-driven biomimetic nanosystem suppresses tumor growth and metastasis through sonodynamic therapy, CO therapy, and indoleamine 2,3-dioxygenase inhibition. *ACS Nano*. 2020;14(7):8985–8999. doi:10.1021/acsnano.0c03833
36. Zhang W, Gong CY, Gao J, Li M, Li Y, Gao J. Tumor microenvironment-activated cancer cell membrane-liposome hybrid nanoparticle-mediated synergistic metabolic therapy and chemotherapy for non-small cell lung cancer. *J Nanobiotechnol*. 2021;19(1):339. doi:10.1186/s12951-021-01085-y